F. Messanelli, E. Frigerio, E. Tescaroli, M. Belan
Flow Separation Control by Pulsed Corona Actuators
Experimental Thermal and Fluid Science, Vol. 105, 2019, p. 123-135
doi:10.1016/j.expthermflusci.2019.03.013

Flow separation control by pulsed corona actuators

Federico Messanelli[a], Edoardo Frigerio[b], Elia Tescaroli[a], Marco Belan[a,*]

Abstract

In this experimental work, corona actuators with triangular tips on their anodes are applied on a symmetric airfoil and tested in the wind tunnel at a freestream velocity of 20 m/s (Re=330k). The actuators are driven by a periodic waveform that improves remarkably their operability with respect to DC driving, increasing also their efficiency. The basic waveform or carrier wave can be modulated introducing a pulsed actuation as usually done for other kinds of plasma actuators. Steady (carrier only) and pulsed (modulated) operation are tested for two actuators, selected out of a larger set previously studied in the laboratory, and compared here with a standard wire-plate corona as reference. The diagnostics include measurements of aerodynamic forces, electrical parameters and local velocities, completed by surface visualizations. Force coefficients and electrical power are used to evaluate the actuators performance in terms of coefficients changes with respect to the smooth airfoil and to the unpowered case, determining also effectiveness parameters in N/W. At the same time, the control mechanism is studied by acquiring boundary layer velocity profiles with plasma off and on, and determining the momentum coefficient of the devices. The passive effects of the unpowered actuators are measured separately and also described by means of surface visualizations. The results confirm the streamwise momentum injection as main mechanism for these actuators, and lead to determine the best flow control achievable by this technique.

---

[a] Dipartimento di Scienze e Tecnologie Aerospaziali, Politecnico di Milano, Milano, Italy
[b] Simscale GmbH, Munich, Germany
∗ Corresponding author. E-mail address: marco.belan@polimi.it

Keywords: flow control - plasma actuators - corona discharge

1. Introduction

In the field of flow control, the non-thermal plasma actuators have been the object of a wide research in the last years. Many actuators operate by energizing the sensitive zones of the flow by inducing a ionic wind; the performance of these actuators in terms of ionic wind velocity and body force is strongly dependent on electrical and geometrical parameters, such as waveform, frequency and amplitude of the applied voltage, gap between the electrodes, material and thickness of the dielectric [1, 2]. An important parameter is the shape of the active electrode, which has a strong influence both on the intensity and the direction of the induced ionic wind. Different spanwise-periodic shapes, such as serpentine [3] and serrated edge [2, 4, 5] have been tested both numerically and in the laboratory.

Most recent works about the influence of electrodes geometry are focused on the DBDs, operated with a wide variety of driving signals. However, also another famous class - the corona actuators - has been studied by introducing anodes provided with periodic triangular tips and discovering that their originally unstable behaviour is greatly improved by this geometry, giving rise to a flow control mechanism of interesting efficiency, at least in applications where the air humidity can be controlled. This has been shown in previous works, where the authors have studied the effects of triangular tips both on DBDs and coronas [6, 7, 8, 9], at the bench in still air and on airfoils in the wind tunnel. The electrodes under test, named multi-tip, have tips of different aspect ratios (length/width), separated from each other or adjacent as in serrated edge geometries. Both DBDs and coronas create low temperature discharges, but their working principles differ. In particular, for multi-tip DBDs the discharge originates along the entire perimeter of the active electrode and the resulting local flow field is inherently three-dimensional, so that the actuator is capable of adding streamwise momentum and working as vortex generator at the same time. For multi-tip coronas instead the discharge originates exclusively from the anode tips and is made of periodic fans spreading from each tip toward the cathode [6, 8]. The relevant control mechanism is related to the intense wall jets arising from each tip, that energize the boundary layer by direct momentum addition in the streamwise direction, to a much larger extent than for a traditional wire-plate corona. In fact, the previous experiments [6, 7] evidence ionic winds from the tips nearly 2 times larger than for a wire at the same conditions, and also in this work the momentum coefficient generated behind a tip results up to 3 times larger.

Up to now, the multi-tip coronas have been tested with DC driving; the present work deals instead with the performance of these devices when operated with a new kind of actuation, based on a positive waveform (carrier wave) that drives the anode with a given frequency f, further improving the operability of the actuators and increasing their efficiency. In this study the corona discharge is used to control a separated flow, and when the separation is complete the main time scale corresponds to the natural vortex shedding. As exposed in the setup description, the carrier frequency f is much larger than the shedding frequency, however a forcing on the proper time scale can be introduced by modulating the carrier wave with a lower frequency $F \ll f$, in order to match the sensitive scales of the flow, as done by means of DBDs in several works dealing with similar problems of separation control [10, 11, 12, 13].

In this experiment, steady (carrier only) and pulsed (modulated) operation are tested for two actuators, selected out of a larger set previously studied in the laboratory, and compared here with a standard wire-plate corona as reference. The 3 actuators are studied by keeping the same anode-cathode gap and the same streamer regime (in turn, this requires the same voltage for the two multi-tips and a higher value for the wire-plate). All the actuators are installed on the nose of an airfoil, with the discharge developing along the suction side from the leading edge line toward the cathode line. The installation on a standard airfoil (NACA 0015) is introduced in order to perform typical tests as in the relevant literature, but the experiment can also be intended as proof of concept in view of a wider field of applications.

In the wind tunnel, the diagnostics include at first measurements of forces and electric power, exploring the effects of different pulse frequencies F and duty cycles D_c. The actuators performance is evaluated in terms of force coefficients changes with respect to the unpowered case and to the smooth airfoil, accounting for the passive effect of the electrodes, that are also studied by means of surface visualizations. Moreover, the influence of the actuators on the local flow is studied by acquiring boundary layer velocity profiles with plasma off and on, and determining the momentum coefficient of the devices.

The results confirm the mechanism of momentum injection for these actuators, the ease of operation with the present driving waveforms and identify the relevant best parameters for separation control.

2. Experiment setup

2.1. Plasma actuators

The corona actuators are installed on the nose of a NACA 0015 airfoil of chord $c = 0.25$ m and span $b = 0.47$ m. Each actuator is assembled on a C-shape insulating insert that fits accurately a corresponding cavity on the airfoil nose. The inserts, 2 mm thick, are obtained by thermoforming PMMA sheets on a mold. Their shape is finished in such a way that the overall NACA 0015 profile is not changed when they are installed on the airfoil as in Fig. 1. The electrodes are made of aluminium tape 0.12 mm thick, except for the anode in the wire-plate configuration which is a 0.1 mm diameter copper wire. As sketched in Fig. 1, they are aligned in such a way as to create the discharge from the leading edge and act early on the boundary layer: in fact, the corona discharge originates only from the tips of the anodes [6], so that its chordwise extension goes from the leading edge to the cathode. The standard wire-plate configuration, considered as a reference, hosts the wire in a groove machined on the leading edge with depth equal to the wire diameter, and originates a distributed discharge across the same gap of the other configurations. The wire is kept tensioned by means of two nylon M3 screws at its ends, secured by drops of retaining compound.

For this study, two corona with multiple tips have been selected from a larger number studied at the bench [6] and in the wind tunnel with DC actuation [8, 9], keeping the wire-plate device as reference. The geometry of the actuators in flat form is shown in Fig. 2: (a) is the standard wire-plate corona C1, (b) is the actuator C6, the best among 15 tested in the wind tunnel for stall control at $U = 15$ m/s, and (c) is the actuator C13, which induces the highest velocity at the bench (the ionic wind for these

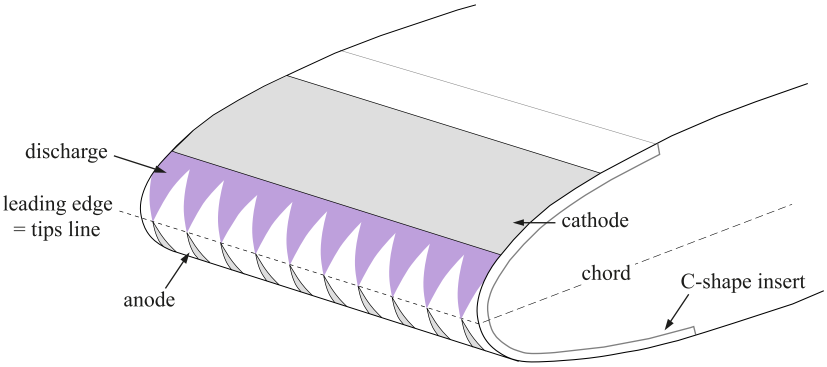

Figure 1: Section of a corona actuator: actual shape and alignment on the airfoil.

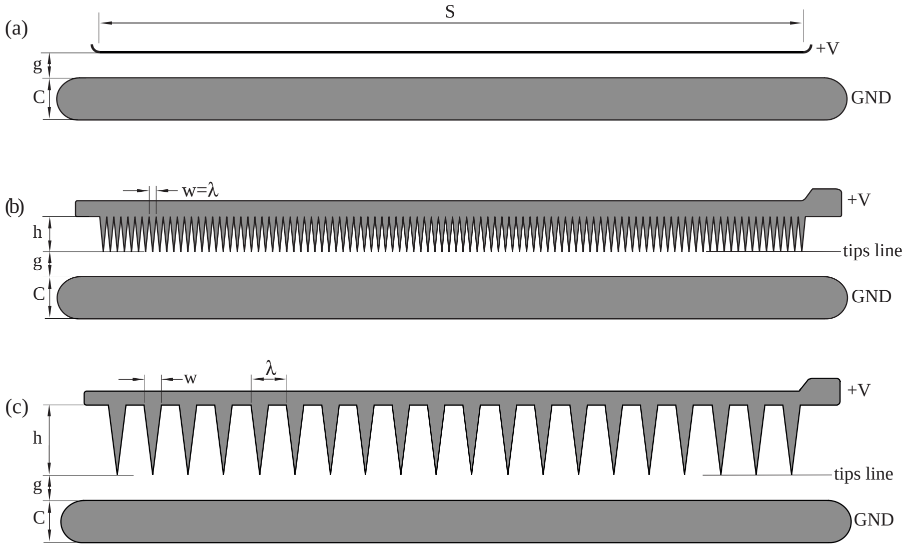

Figure 2: Geometries of the 3 coronas in flat form: (a) straight wire-to-plate C1; (b) multi-tip, serrated C6; (c) multi-tip, separated tips C13.

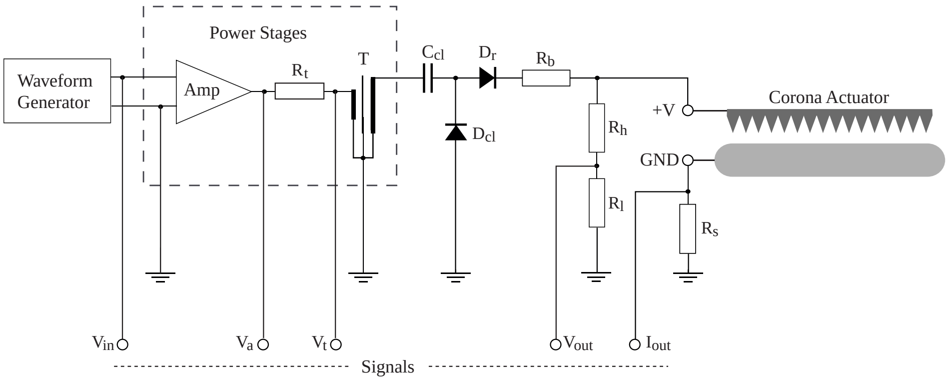

Figure 3: Electrical setup for the corona actuators.

actuators ranges from 2 to 4 m/s). The codes C** are consistent with the naming convention used in the cited works.

All the actuators have a working span $S = 400$ mm. The gap between anode and cathode is always $g = 15$ mm and the cathode has a chordwise length $C = 25$ mm. The complete geometric parameters of the anodes are listed in Table 1, that reports the height h and width w of the tips, the tips density $n = N/S$ (tips number per unit length), the sharpness $r = h/w$ and the inter-tip distance $\lambda = 1/n$.

Table 1: Corona actuators under test

Name	h [mm]	w [mm]	$n = N/S$ [m^{-1}]	$r = h/w$	$\lambda = 1/n$ [mm]
C1	0	–	–	0	–
C6	20	4	250	5	4
C13	40	10	50	4	20

The coronas are driven by an oscillator+amplifier+transformer system capable of 100 W at $V_{pp} = 20$ kV, already used for DBD driving [6, 9] and purposely modified in this work, as shown in the electrical diagram of Fig. 3: the desired waveform for the actuators is obtained by connecting the transformer output to a clamper stage (D_{cl} and C_{cl}=1 nF), a rectifier D_r and a ballast resistor $R_b = 4.4$ MΩ. The diagram includes the measurement section, made of a 1:1000 voltage divider (R_h and R_l, load 47 MΩ) and a shunt resistor ($R_s = 68$ or 100 Ω) connected to a 350 MHz oscilloscope with 20 Mrecords/trace.

The principle of operation can be sketched as in Fig. 4: owing to the circuit of Fig. 3, the waveform to the actuator is created by translating the AC output toward positive voltages by an offset equal to the half-amplitude of the carrier wave. Moreover, acting on the signal generator, the basic waveform of frequency f can be modulated by a lower frequency F creating pulse trains of duty cycle D_c. In what follows, the continuous wavetrain with $D_c = 1$ or 100% is indicated as *steady actuation*, in contrast to the modulated one, named *pulsed actuation*. Figure 4 evidences also a peculiar property of this operation mode: since the ignition voltage V_i is relatively high, a waveform of this kind excites the discharge only for short time periods, represented by the wave crests above V_i during the active phase of the modulation (in the inactive phase the voltage is not zero, but well below the ignition value, so that the actuator is completely off).

A common problem for DC driven corona is their poor operating stability, because once the voltage exceeds the ignition value V_i, a small increase can easily lead to arc discharges, i.e. the ignition and spark voltages V_i and V_{arc} are very close each other, in the order of 200 V for the present geometries. This problem is solved by the new operating mode, even with the bare carrier frequency without modulation: all the actuators become more stable and their working interval V_i to V_{arc} can grow up to 3 kV, allowing a simpler adjustment of the working point in laboratory tests. Also the operating range with respect to the ambient humidity improves, with stable operation up to 65%, and this humidity level could presumably grow on actuators with non hygroscopic dielectric.

The dependence on the carrier frequency f has been checked over the range 500Hz to 2.5kHz, compatible with the power system response: in this frequency band, the ionic wind increases moderately

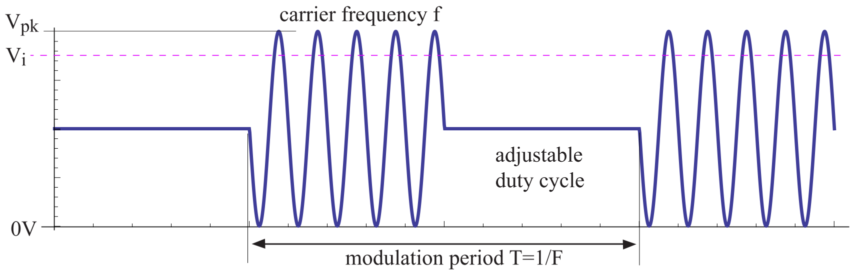

Figure 4: Voltage waveform and principle of operation for pulsed coronas: the actuator is turned on cyclically by the wavecrests trains above the ignition voltage V_i.

with f, whereas the power consumption is minimum in the interval $800 \leq f \leq 840$ Hz and grows very rapidly for $f > 1$ kHz. For the actuators under test, indicating as W_0 the input power at $f = 800$ Hz, the consumption can grow up to 5.9 W_0 by lowering f to 500Hz and up to 11.3 W_0 by increasing f to 2 kHz. The above data indicate that the power system coupled with the load exhibits a resonant behaviour similar to the transformer-DBD systems [17], and this led to set a carrier frequency $f = 800$ Hz in order to keep the system at a good efficiency level.

The working voltage has been set, as for DC operation, at the highest possible value without sparks, i.e close to V_{arc}; for the multi-tips this corresponds to peak values $V_{pk} = 13.0$ kV. Under these conditions the ionic wind at the bench has been measured as function of the wall distance by means of a small pitot probe, with the same setup used for DC operation [6]. The curves obtained with DC supply have been substantially reproduced here, but the velocities are scaled by a factor 0.7. However, in the present experiment these velocities are time averaged values, whilst the instantaneous values should be considered as pulsing over larger values: in fact, the resulting flow control capability is better than for DC operation, as will be shown in §3.

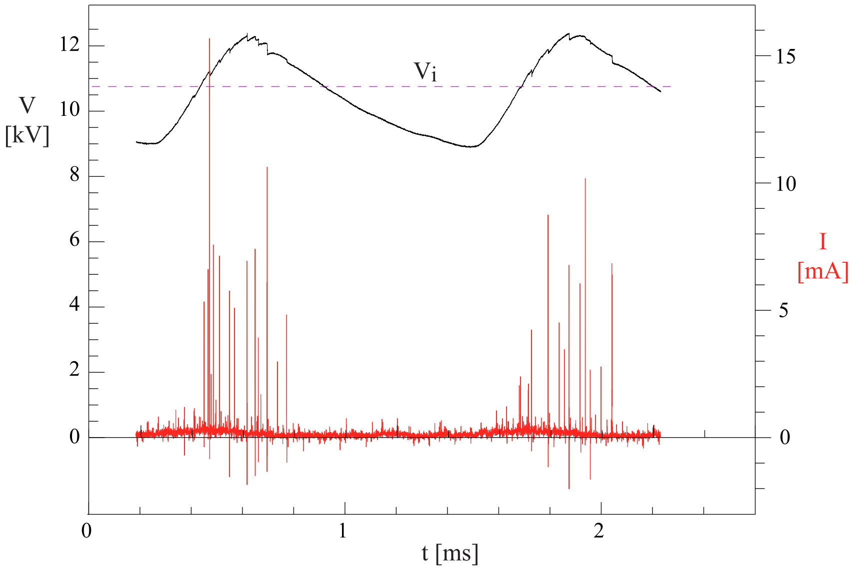

Figure 5: Voltage and current of the corona C6 operated at low power conditions, freestream velocity U =10 m/s. The dashed line is the ignition voltage V_i.

The actual behaviour of a corona actuator connected to the circuit of Fig. 3 is more complicated than for a simple resistive load: an example of the real trends of voltage and current along 2 carrier periods during the active phase of the modulation can be seen in Fig. 5. The voltage curve does not drop sinusoidally after each peak because of the inherent capacity of the actuator and the circuit; however the working principle, as expected, is a sequence of discharges corresponding to the peaks of voltage. In detail, when the voltage overcomes the ignition value V_i, a current burst made of several streamers appears, and each streamer causes a fast and small voltage drop. The signals depend also on the freestream velocity, as usual for corona discharges: for increasing velocities U, the actuator current grows slightly and the ignition voltage diminishes. In particular, for the multi-tip C6 and C13 the ignition voltage V_i decreases from 11.7 kV at $U = 0$ m/s to 10.6 kV at $U = 20$ m/s, whereas for the wire-plate C1 the values of V_i are higher, in the range 13.1 kV to 11.5 kV.

The signals in Fig. 5 have been acquired on actuator C6 at $U = 10$ m/s, setting a V_{pk} lower than 12.5 kV, in order to avoid intense streamers that could give rise to transient sparks and high, potentially destructive voltage pulses on the oscilloscope input. For this reason the current and the consumed power are quite low in this example; however, for the effective aerodynamic tests, the current values are much higher and obtained by setting $V_{pk} = 13.0 \pm 0.25$ kV for the multi-tips and $V_{pk} = 14.1 \pm 0.25$ kV for C1 (averages of several peaks), since the wire-plate requires a higher voltage to achieve the same operating regime. The accuracy of power measurements is improved in the present work by acquiring also the voltage and current waveforms on the primary winding of the transformer (see V_a, V_t outputs in Fig. 3) and – accounting for the transformer efficiency and the circuit losses – comparing the relevant power to the one read at the actuator. However this double check was done only at low power values, for safety reasons: actually, in order to protect the oscilloscope from the rare but undesired transient sparks, the higher power levels were measured only at the primary winding. The accuracy is in the order of ±0.35 W for C1 and ±0.8 W for C6 and C13.

2.2. Wind tunnel, airfoil and balance

The experiment has been carried out in an open-circuit wind tunnel in the aerodynamics laboratory of the Aerospace Department (DAER) of Politecnico di Milano, already described in [8, 9]. A sketch of the setup is presented in Fig. 6: the test section is 0.5×0.7 m^2 in cross section and 2 m in length; the maximum velocity is 25 m/s and the maximum turbulence level is 0.5%. The airflow velocity in the test section during the experiment was set to 20 m/s, corresponding to a nominal Reynolds number, based on the chord length, of 330k. The NACA 0015 airfoil (chord × span 0.25×0.47 m) with interchangeable inserts for the actuators was already used and described in [8, 9]. End plates made in PMMA are located at the two lateral edges of the airfoil, in order to limit end effects and recover 2D behaviour; however, due to technical limitations in the airfoil rotation, the end plates are not large enough to completely eliminate 3D effects. The airfoil is connected to the external aerodynamic balance by two lateral trunnions. In the present setup, they have been improved in order to minimize the errors on force measurements, since it was observed in previous tests at $U > 18$ m/s that for high angles of attack the large moment on the airfoil may cause undesired rotations, very small but capable of affecting the measurement accuracy. The angle of attack α is set by means of a high quality positioning system designed for optical devices, with accuracy ±0.005°. The residual transversal velocities in the test section (crossflow) and the deformation of the airfoil supports may affect the desired α setting, however the overall accuracy of α remains better than ±0.1°. This is the smallest angle for which a change of lift and drag can be consistently measured.

The balance is made of 4 HBM S2M load cells, symmetrically located on the two sides of the test chamber. Two cells are sensitive to horizontal loads (range 50 N, accuracy of ±0.01 N), the other two are sensitive in the vertical direction (range 100 N, accuracy ±0.02 N). The balance, intended as a mechanical system made of the 4 cells together with the other components, has been calibrated by applying known loads, according to the standard procedures [14] and accounting for the combined effects of lift and drag. Also the long term stability is checked yearly. The overall accuracies of the force coefficients declared at the end of this section rely on these procedures.

In this kind of measurements, the electromagnetic field induced by the plasma discharge can easily affect the weak signals of the balance, therefore a conditioning system has been purposely built, making use of high performance operational amplifiers and a very stable power supply. The balance outputs are connected to the system through double shield differential lines of short length. The conditioner output, amplified by an adjustable factor up to 1000, is then connected to the digital acquisition system, obtaining in this way a good rejection to electro-magnetic disturbances. The analog signals of loads have been acquired and digitally converted at 4 kSamples/s with 16 bit depth. The signals have been averaged over a time of at least 10 s, in order to obtain a good accuracy even in the postcritical (stall) range of attack angles, whereas a shorter time would be enough at low and moderate angles. The freestream velocity is measured by means of the pressure jump across the converging section of the tunnel, read through suitable wall taps.

Lift and drag curves have been acquired for increasing values of α, in the range $0° \leq \alpha \leq 35°$; in each measurement, the angle of attack was always set first to 0° and then taken to the desired value, in order

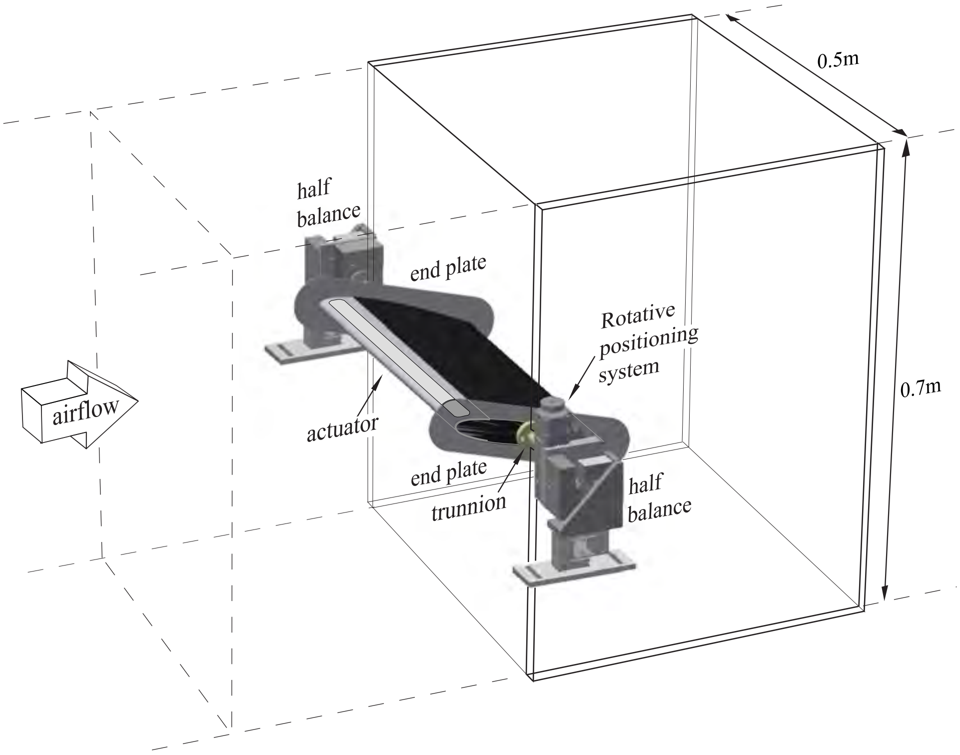

Figure 6: Experimental setup: airfoil, balance and parts of the tunnel walls. Interchangeable panels permit visualizations and access for pressure probes.

to prevent hysteresis effects. In terms of standard deviations, the resulting overall uncertainties on the force coefficients c_l and c_d at U=20 m/s are $(\sigma_{cl}, \sigma_{cd}) = (0.0061, 0.0027)$. These values represent the worst operating conditions, corresponding to the stalled airfoil, whereas for small angles of attack the values of σ_{cl} and σ_{cd} are lower. Solid, wake blockage and streamline curvature corrections have been applied to the results, following the procedure described in [14, 15]. In the results section, all the data, and in particular the force coefficients c_l and c_d, are directly presented in corrected form (for high blockages, the effective Reynolds number becomes 340k).

2.3. Boundary layer diagnostics

To characterize the boundary layer of the baseline flow and the passive effects of the unpowered actuators, surface visualizations have been performed on the airfoil in several configurations. The china clay technique has been chosen, because the pigment is mixed with a light carrier liquid, that evaporates rapidly and makes the model and the actuators much easier to clean with respect to other diffused techniques. These visualizations are realized by accessing the test section of Fig. 6 from above, with the airfoil set to positive angles of attack. To increase the image contrast, the surface under study is painted with matt black. After the wind tunnel is turned off, the airfoil surface has been photographed acquiring images with resolution 5568x3712 and depth 24 bit in order to retrieve the desired flow details.

Local velocity measurements have been acquired in the boundary layer region downstream of the actuators, with plasma off and on. The velocities have been obtained by traversing a total pressure probe with outer diameter $d_p = 0.4$ mm, locally parallel to the airfoil surface. The traversing system permits also spanwise movements and is mechanically decoupled from the test section frame, in order to improve the positioning accuracy. In the setup of Fig. 6, the probe is held from above and the measurements are performed with the airfoil set to positive angles of attack. The pressure values are acquired by transducers of accuracy ±0.1% with full scales 254 or 1270 Pa and are corrected for the wall and shear effects where necessary. The data are acquired at 25 kSamples/s with 10 bit depth and averaged over a time much larger than the time constant of the probe-line-transducer system. The resulting velocities have accuracies in the order of ±1.5% excepting the points lying at less than $2\,d_p$ from the wall, where the accuracy can worsen up to ±18% and not repeatable measurements have been omitted.

3. Results

3.1. Baseline flow and passive effects of the actuators

With regard to the wind tunnel testing, the effectiveness of the actuators will be discussed in terms of variations of lift and drag by comparing the performance of the bare airfoil and the actuated one, with plasma off and on. In fact, also the unpowered actuators can affect the airfoil aerodynamics [20], and this point is treated in the present section in order to give a complete description of the phenomenon under study. The baseline flow is reproduced here by means of a C insert without electrodes mounted on the leading edge, and the acquisition of the relevant lift and drag curves vs. α gives the reference data. These data are strictly valid only with the present setup, because of the three-dimensionality of the real flow around a wind tunnel airfoil, so that very different values can be found in literature. For example, the spreading of maximum lift values reported for the 0015 airfoil in different experiments on the narrow interval 220k$\leq Re \leq$260k ranges from c_{lM}=0.95 to more than 1.2, depending on the different aspect ratios, end or splitter plates used in each work [11, 18, 19].

All the actuators considered here do not modify the lift curve for small angles of attack, whereas their effect becomes visible when α approaches the critical (stall) value α_c. At the present Reynolds number the original boundary layer on the smooth profile is laminar at the leading edge, then it forms a typical recirculation bubble and finally, downstream of an unsteady reattachment, the transition to turbulence takes place. As α grows, the laminar zone becomes progressively shorter, and for α close to α_c the flow is laminar only within a small region shorter than 15 mm from the leading edge, including the bubble, whilst downstream of this zone the transition to turbulence takes rapidly place. This can be predicted numerically (XFoil simulation [21]) or visualized as in Fig. 7, that depicts the boundary layer state for $\alpha = 13.5°$.

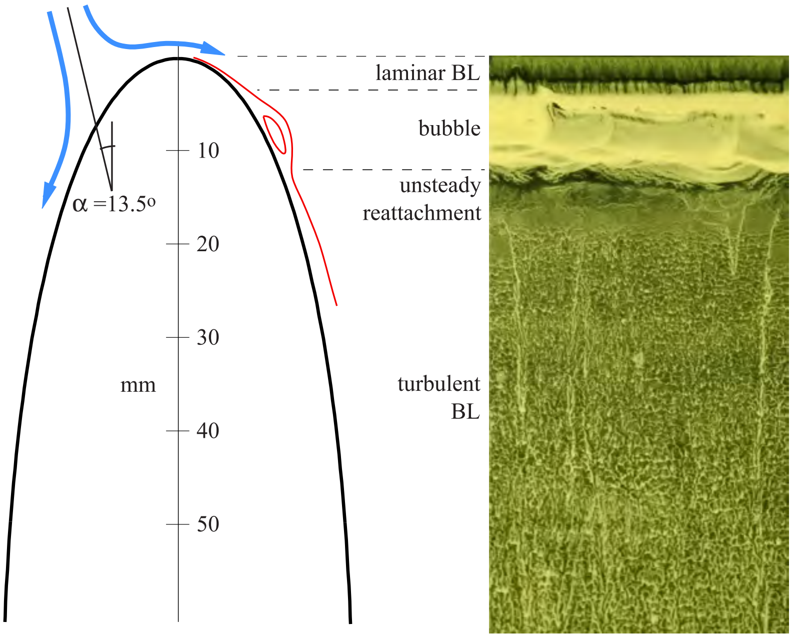

Figure 7: Surface visualization of the baseline flow on the suction side at mid-span, for α=13.5° at U =20 m/s or Re=330k. In the left side sketch (red lines), the BL thickness is enlarged for clarity.

The unpowered electrodes on the airfoil surface can generally give measurable effects, since their 0.12 mm thickness, which ensures a reliable duration to the tips, is not negligible with respect to the early BL thickness, and even the 0.1mm wire of the reference actuator, although placed in a suitable groove, can affect the BL development. In fact, for $\alpha \sim \alpha_c$ along the smooth airfoil, the baseline displacement thickness δ^* varies approximately between 0.05mm to 0.5mm along a 40mm extension from the leading edge, which is the main region of influence of the discharge. The above values of δ^* can be predicted by XFoil, and the largest values in the order of 0.5mm can also be confirmed by the baseline velocity profiles measured by the pitot probe used in this work. The passive effects of these actuators can be outlined by

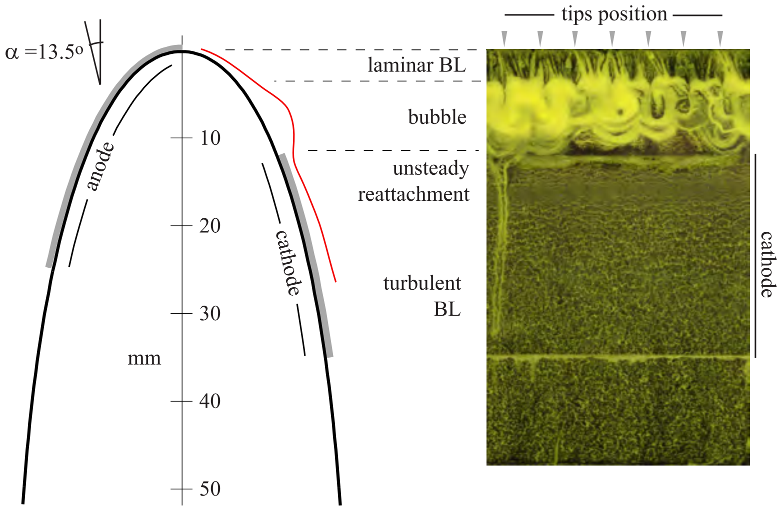

Figure 8: Surface visualization on the suction side for the unpowered actuator C6, mid-span for α=13.5° at U =20 m/s. In the left side sketch, electrodes and BL thicknesses are enlarged for clarity.

observing that for $\alpha \sim \alpha_c$, the anodes (Fig. 1) lie in the accelerated zone between the stagnation point and the leading edge, whilst the cathodes lie in the adverse gradient zone downstream of the leading edge. Since cathode and gap are the same for all the coronas, the passive effects of these actuators, already treated by the authors in [8], are relatively similar to each other and the lift curves of different coronas are not much dispersed with respect to the reference. In detail, the tips upstream of the leading edge create in the laminar zone a row of thin wakes that affect the bubble, increasing its unsteadiness and promoting a faster transition to turbulence. The transition improvement is created also by the wire of C1, but with a more uniform effect along the span. As regards the cathode with its straight borders, it lies in a region which is already transitional and fairly thick in the baseline flow, so it does not seem to alter remarkably the BL properties. This is visible for example in Fig. 8, that refers to corona C6 for $\alpha = 13.5°$. As a general consequence, all the unpowered coronas favour the transition in this way, creating small lift increases for $\alpha \sim \alpha_c$. Small stall delays and lift increases in deep stall have also been observed.

3.2. Performance parameters

The performance of the actuators under test can be evaluated from two different points of view: I) focusing on the total or absolute variations obtained by modifying a smooth airfoil of coefficients (c_l, c_d) by introducing an actuator and switching it on, what gives new force coefficients $(c_{l,on}, c_{d,on})$; II) studying the relative changes occurring when a given actuator, already installed, is switched on. This variation, $(c_{l,off}, c_{d,off})$ to $(c_{l,on}, c_{d,on})$, is exclusively due to the plasma discharge. For the lift coefficient, a sample sketch of these curves can be seen in Fig. 9. Depending on the selected approach, the parameters useful to the actuators characterization can be defined in different ways, as explained in what follows.

A first parameter can be introduced by measuring the lift increase at critical point, as in [8, 9]: following the two approaches I) and II), the total variation (smooth to plasma actuated airfoil) is

$$\Delta c_{lMt} = \frac{c_{lM,on} - c_{lM}}{c_{lM}} \tag{1}$$

whereas the relative variation (plasma off to plasma on) is

$$\Delta c_{lMp} = \frac{c_{lM,on} - c_{lM,off}}{c_{lM,off}}. \tag{2}$$

These parameters will be presented in percentage form. They are local parameters, related to the critical points of the lift curves, and the actuators characterization can be completed by introducing integral or global parameters that describe the displacements occurring to the whole lift and drag curves. Regarding

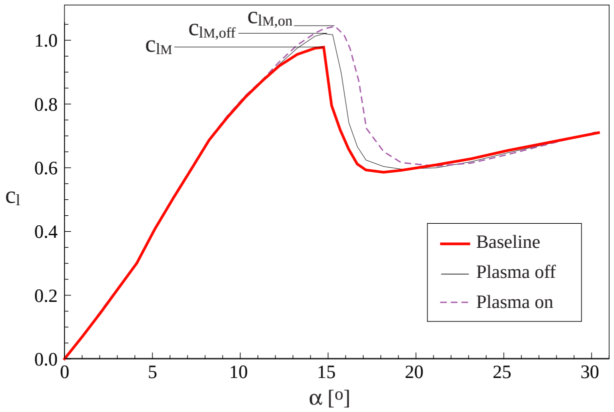

Figure 9: Progressive variations of the lift coefficient: thick line = baseline c_l curve, smooth airfoil; thin line = $c_{l,off}$ curve, airfoil with unpowered actuator; dashed line = $c_{l,on}$ curve, airfoil with actuator on

the variation from baseline to plasma on conditions (I), the mean lift increase can be defined as

$$<\Delta c_l>_t \quad = \quad \frac{\int_0^{\alpha_M} (c_{l,on} - c_l)\, \mathrm{d}\alpha}{\int_0^{\alpha_M} c_l\, \mathrm{d}\alpha} \tag{3}$$

whereas the part due only to the plasma discharge (II) is expressed by

$$<\Delta c_l>_p \quad = \quad \frac{\int_0^{\alpha_M} (c_{l,on} - c_{l,off})\, \mathrm{d}\alpha}{\int_0^{\alpha_M} c_{l,off}\, \mathrm{d}\alpha} \; . \tag{4}$$

In a similar way, the mean drag reduction for the total (I) and plasma effect (II) are

$$<\Delta c_d>_t \quad = \quad \frac{\int_0^{\alpha_M} (c_d - c_{d,on})\, \mathrm{d}\alpha}{\int_0^{\alpha_M} c_d\, \mathrm{d}\alpha}, \tag{5}$$

$$<\Delta c_d>_p \quad = \quad \frac{\int_0^{\alpha_M} (c_{d,off} - c_{d,on})\, \mathrm{d}\alpha}{\int_0^{\alpha_M} c_{d,off}\, \mathrm{d}\alpha} \; . \tag{6}$$

All the above integrals are evaluated over the same domain $0 \leq \alpha \leq \alpha_M$. As visible in Fig. 9, the main contribution to these parameters is due to the large distance between curve pairs (base–on or off–on) in the postcritical range, and above sufficiently high values of α, the integrals cease to depend on α_M, since the curves return to coincide within the accuracy level; in order to obtain reliable results, the above parameters are evaluated over an interval extended to $\alpha_M = 35°$.

Another field of characterization for the actuators is their effectiveness in terms of power. Focusing on stall control, the actuators can be compared on the basis of two parameters already introduced in [8]: the critical lift effectiveness

$$\varepsilon_{lct} \quad = \quad \frac{\Delta L_{Mt}}{W_c} = \frac{L_{M,on} - L_M}{W_c} \; , \tag{7}$$

where $L_{M,on} - L_M$ is the change in maximum lift from smooth to actuated airfoil and W_c the relevant power consumption at the stall inception; and the mean lift effectiveness

$$\varepsilon_{lmt} \quad = \quad \left\langle \frac{\Delta L_t}{W_e} \right\rangle = \int_0^{\alpha_M} \frac{L_{on} - L}{W_e}\, \mathrm{d}\alpha \; , \tag{8}$$

which is the mean ratio of total lift increase to electric power consumption.The parameters $\varepsilon_{lct}, \varepsilon_{lmt}$ are based on total variation of kind (I) and it is straightforward to define the corresponding parameters for the pure plasma effect (II), namely $\varepsilon_{lcp}, \varepsilon_{lmp}$. All the above parameters are expressed in N/W, but they can become dimensionless by referring to an idealized flight test, where an airfoil lifts a load with vertical velocity U_y and the relevant lifting power is $U_y L$. For instance, the parameters $\varepsilon_{lct}, \varepsilon_{lmt}$ lead in this way to the power saving ratios

$$\begin{aligned} \eta_{lct} &= U_y \Delta L_{Mt} / W_c && (9) \\ \eta_{lmt} &= (U_y/\alpha_M) \langle \Delta L_t / W_e \rangle \, . && (10) \end{aligned}$$

Values larger than 1 for these dimensionless parameters would indicate that a given electrical power successfully controls a larger mechanical power.

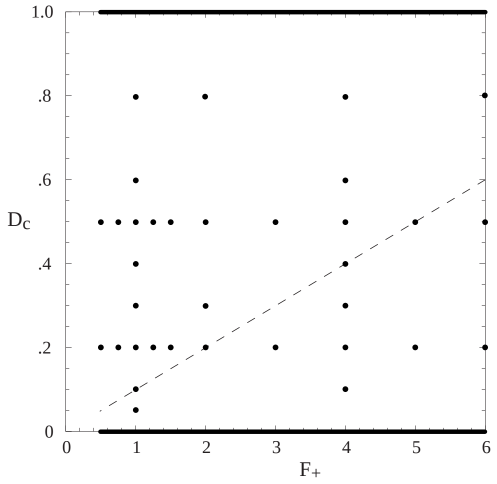

Figure 10: Space parameter exploration: black points and thick lines represent the testing conditions (top line = steady actuation; bottom line = no actuation). Below the dashed line the pulse duration is shorter than the carrier period of 1/800 s.

For each actuator, all the performance parameters can be measured under steady or different pulsed actuations, by selecting modulation frequency F and duty cycle D_c for each test. This generates a large amount of data that will be presented in a reasonable space in the next section, by evidencing the physically meaningful results. Expressing the modulation frequency in dimensionless form as $F_+ = Fc/U$, scaled on the airfoil chord and the freestream velocity, the criterion adopted to explore the parameter space F_+, D_c is as follows: considering the existing literature and the outcomes of preliminary measurements, the test grid has been set as in Fig. 10, mainly focused on a low frequency $F_+ = 1$, a high $F_+ = 4$, and on two duty cycles $D_c = 0.2$ and 0.5; the map is then completed by some other values of (F_+, D_c), by the top line (steady actuation) and by the bottom line (actuator off). For each (F_+, D_c) condition, the force coefficients as functions of α are measured, leading to a total of 36 tests for each actuator (black points and thick lines in figure). For high F_+ and low D_c the pulse duration can also be shorter than the carrier period: in Fig. 10 these points lie below the dashed line $D_c = F/f$.

3.3. Force measurements

The lift increase due to the plasma discharge at stall inception, expressed by the parameter Δc_{lMp}, is visualized as function of F_+ and D_c in Fig. 11, and shows that for all the actuators this parameter grows quite regularly as D_c increases: the optimal lift increase is always obtained for $D_c = 1$ (steady actuation). Here the measured quantities are shown by means of interpolated surfaces plotted over the (F_+, D_c) domain: this method permits an easier readability, with surfaces acting as a guide to evaluate the actual data values, whereas the best numerical values are reported in detail in Table 2 below. In general, the maps in Fig. 11 show that the pulsed actuation is not so effective in increasing the maximum lift, a result that has already been evidenced in literature about pulsed DBDs [12, 13]. On the other hand, the pulsed actuation works much better in the postcritical range of α, as it will be shown below. In particular, the figure shows also that the two multi-tips perform much better than the wire-plate C1, and C6 seems less dependent on the duty cycle variation.

The maps of Fig. 11 could be easily produced also for the total effect in maximum lift increase Δc_{lMt} (see Table 2 for the numerical values). However, the maps of Δc_{lMt} and Δc_{lMp} have similar morphologies,

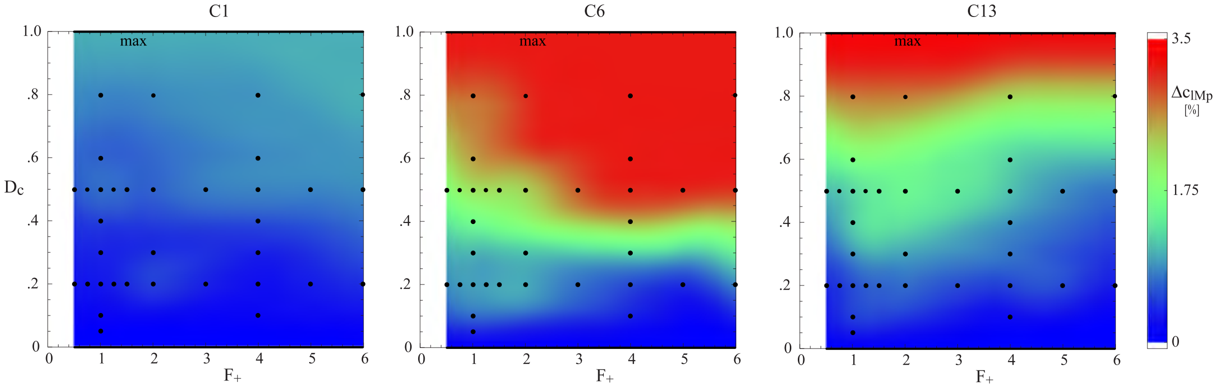

Figure 11: Maps of Δc_{lMp} as function of F_+ and D_c. All the maxima are obtained for $D_c = 1$.

with minima and maxima on the same locations, because their data points are linearly dependent from the Δc_{lMp} values, i.e. from definitions (1) and (2) it is easy to show that

$$\Delta c_{lMt}(F_+, D_c) = A\,\Delta c_{lMp}(F_+, D_c) + B \; , \tag{11}$$

where A and B are constants, specific of each actuator and independent of F_+ and D_c. In general, each total parameter (base to plasma on) is related to the corresponding discharge effect parameter (plasma off to on) by this property.

The detailed data about the maximum lift increases are collected in Table 2, where the actuators are listed in descending order of relative (off-on) increase Δc_{lMp}. Next to this column, the table reports the total increase Δc_{lMt} including the passive effect, then the working conditions (F_+, D_c) for which those maxima are measured (optimal performance with steady actuation is indicated by $D_c = 1.0$). The accuracy of Δc_{lMt} and Δc_{lMp}, that are normalized differences of similar values, is in the order of ±1.4%. Each row is completed by the power consumption per unit length W_c/S and the critical lift effectiveness defined in §3.2, calculated both for the plasma off–on effect as ε_{lcp} and for the total effect as ε_{lct}. In particular, the multi-tips C6 and C13 exhibit very similar off-on increases Δc_{lMp}, much larger than for the standard wire-plate C1. In the next section the flow behind the actuators will be studied by acquiring boundary layer velocity profiles, and the results show that C13 and C6 have also a higher momentum coefficient c_μ with respect to C1. As regards the total increases Δc_{lMt}, they are larger for all the actuators, because the passive effect is favourable, as explained in §3.1. Here the best total Δc_{lMt} is given by C6 that was also the best device in previous tests at 15 m/s with DC supply [8].

Table 2: Stall inception performance. Best values of maximum lift increases (on-off and total), with working conditions, power and effectiveness parameters.

Actuator	Δc_{lMp} [%]	Δc_{lMt} [%]	F_+	D_c	W_c/S [W/m]	ε_{lcp} [N/W]	ε_{lct} [N/W]
C13	3.4	5.4		1.0	9.2	0.27	0.41
C6	3.2	6.5		1.0	14.7	0.16	0.31
C1	1.0	5.1		1.0	5.3	0.13	0.65

The power consumption should be read while recalling that in multi-tip coronas the discharge originates only from the tips and not from the whole electrode contour, as sketched in Fig. 1 and visualized in [6]. Indeed, the power consumption seems directly related to the tips number, N=20 for C13 and N=100 for C6. Moreover, the power/(tips number) ratio W_c/N is 0.059 W/tip for C6 and 0.18 W/tip for C13, indicating that the comparable performance of C13 and C6 depends on balancing effects: the well spaced fan discharges of C13 are more intense, whereas the discharges of C6 are less intense but much more numerous. Clearly, W_c/N cannot be defined for the wire-plate C1: as the other coronas, it works by injecting streamwise momentum in the boundary layer, but instead of fan shaped discharges starting from tips it creates an incoherent set of microdischarges in the wire–cathode gap.

As regards the effectiveness of the discharge ε_{lcp}, the best value is given by C13 with 0.27N/W. It is worth to note that all the ε_{lcp} values at 20 m/s are in the same order as those recorded for the same actuators driven by DC at 15 m/s [8], despite the higher velocity of the present tests, that requires a more effective actuation; this confirm the better performance of the coronas when operated with the present waveform. Moreover, it is easy to show that the parameters ε_{lct}, ε_{lcp} are better than the corresponding ones for comparable DBDs [16], i.e. devices giving c_l increases in the same order of the coronas. The total effectiveness ε_{lct} is calculated from the total lift increase Δc_{lMt} which is favoured by the passive effect, so that all the ε_{lct} values are higher than the relevant ε_{lcp} for the discharge alone.

To characterize the deep stall performance of the actuators, the integral parameter $<\Delta c_l>_p$ and $<\Delta c_l>_t$ are more useful because they depends primarily on the lift curves variations in the postcritical range of α. The maps of $<\Delta c_l>_p$, that represents the pure discharge effect, are visualized as function of F_+ and D_c in Fig. 12, whereas the best numerical values are reported in detail in Table 3 below, including the total data $<\Delta c_l>_t$ that account for the passive effect.

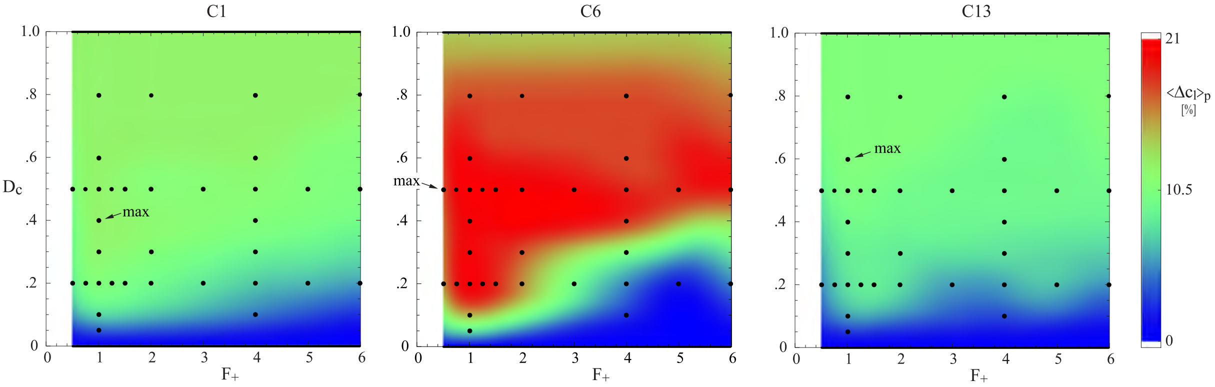

Figure 12: Maps of $<\Delta c_l>_p$ as function of F_+ and D_c. The maxima are explicitly indicated on each map.

In Table 3 the actuators are listed in descending order of mean lift increase $<\Delta c_l>_p$, i.e. the relative (off-on) variation due exclusively to the plasma discharge. The next column reports the corresponding total mean lift increase $<\Delta c_l>_t$, which includes the passive effect. The accuracy of $<\Delta c_l>_t$ and $<\Delta c_l>_p$ is in the order of $\pm 1.2\%$. Then, the table presents the columns for the relevant working conditions (F_+, D_c), the electrical data W_e/S and the mean lift effectiveness defined in §3.2, calculated for the plasma off–on effect (ε_{lmp}) and for the total effect (ε_{lm}).

Table 3: Deep stall performance. Best values of mean lift increases (on-off and total), working conditions, power and effectiveness parameters.

Actuator	$<\Delta c_l>_p$ [%]	$<\Delta c_l>_t$ [%]	F_+	D_c	W_e/S [W/m]	ε_{lmp} [N/W]	ε_{lmt} [N/W]
C6	20.3	24.3	0.5	0.5	7.9	1.8	2.1
C13	10.5	20.8	1.0	0.6	5.5	1.3	2.6
C1	11.8	20.4	1.0	0.4	2.1	3.9	6.7

The data of Fig. 12 and Table 3 reveal that pulsed actuation is effective in deep stall control, since the best performance corresponds to $D_c < 1$ for all the actuators, in contrast to the maximum lift increase which requires steady actuation (Table 2). Moreover, also the anode geometry becomes here particularly important: it is evident that moving from early to deep stall, C6 maintains a good performance, whilst C13 drops to values comparable to the ones of C1, which continues to give a modest performance. As before, the total parameter $<\Delta c_l>_t$ expressing the baseline–plasma on variation gives larger lift increases for all the actuators, and even in this column C6 is the most performant.

The pulsed actuation is the object of a wide literature, mainly focused on DBDs, and it is known that it modifies the natural vortex shedding, driving spanwise-oriented vortex structures [10], with a stall control capability greatly improved when F_+ matches the proper scale of the flow. This phenomenon could help in interpreting the present data, since the wire of C1 and the numerous and dense tips of C6 could be capable of releasing spanwise vortex structures better than the isolated tips of C13. In turn, the superiority of C6 on C1 would simply arise as a consequence of its larger control capability, already evidenced in steady operation mode. The complete identification of the flow structures goes beyond the scope of this work, however the boundary layer velocity profiles and the resulting momentum coefficients c_μ presented in the next section show that C13 gives high local c_μ only downstream of its isolated tips, whilst the largest spanwise-averaged c_μ is given by C6, supporting the hypothesis mentioned above.

With respect to the literature data, where the DBDs are driven also with very short duty cycles, the coronas seem to work better with higher D_c values, however a deeper data analysis shows that this parameter can be reduced, at least on properly selected actuators, maintaining a good performance and leading also to a better effectiveness. In fact, the map of $<\Delta c_l>_p$ as function of (F_+, D_c) for C6, visible in Fig. 12, contains a wide region where $<\Delta c_l>_p$ is larger than 15%; the top value $<\Delta c_l>_p = 20.3\%$ is found for $(F_+, D_c) = (0.5, 0.5)$ but it is also possible to set the duty cycle down to the point $(F_+, D_c) = (1, 0.1)$, where the lift increase maintains a high value $<\Delta c_l>_p = 18.0\%$ and the efficiency ε_{lmp} reaches 7.9 N/W. This point belongs to a vertical region of good performance centered on $F_+ = 1$, which is also the most frequently reported value for best stall control.

The detailed behaviour of corona C6 can be observed in Fig. 13, that compares lift and drag curves for steady and pulsed actuation, superimposed to the baseline and plasma off curves. The passive effect of C6 is weak, and it is evident that a steady actuation leads to a large variation of the lift curve: this case corresponds to the top line in Fig. 11 and 12, and to a value $<\Delta c_l>_p = 13.9\%$. The introduction of a modulating frequency still improves the performance in deep stall, but at the price of a slightly lower increase in maximum lift Δc_{lMp}. The pulsed actuation case shown in Fig. 13(a) refers to the low duty cycle condition $(F_+, D_c) = (1, 0.1)$ explained above, with $<\Delta c_l>_p = 18.0\%$, i.e. not the best $<\Delta c_l>_p$ but a highly effective condition in terms of N/W. In Fig. 13(b) the corresponding impact on drag can be observed: the steady actuation reduces the drag in a useful range of α, whereas the pulsed actuation, after a certain reduction in early stall, create a moderate c_d increase in deep stall. This is not surprising, since the working point (F_+, D_c) in Fig. 13 has been selected to optimize the lift, and in general pulsed actuation can not optimize lift increase and drag reduction at the same time, as exposed in the following part which deals specifically with drag measurements.

The drag reduction performance is evaluated here by means of the integral parameters $<\Delta c_d>_p$ and $<\Delta c_d>_t$ after Eqs. (5) and (6). The maps of $<\Delta c_d>_p$, representing the pure discharge effect, are visualized as function of F_+ and D_c in Fig. 14, whilst the best data are presented in Table 4, with the actuators listed in descending order of mean drag reduction $<\Delta c_d>_p$. The next columns reports the total reduction $<\Delta c_d>_t$ and the relevant working conditions (F_+, D_c). The accuracy of $<\Delta c_d>_p$ and $<\Delta c_d>_t$ is in the order of ±1.5%.

Table 4: Best values of mean drag reduction (on-off and total) and working conditions.

Actuator	$<\Delta c_d>_p$ [%]	$<\Delta c_d>_t$ [%]	F_+	D_c
C6	8.4	10.5		1.0
C13	7.0	10.7		1.0
C1	4.0	5.0	4.0	0.2

The largest drag reduction $<\Delta c_d>_p$ is given by C6, followed by a comparable value for C13 and a lower value for C1. The two multi-tip work at best with steady actuation, but Fig. 14 shows that, when operated by pulsed actuation, all these devices work better with high values of F_+, well above 1. The advantages of a fast modulation F_+ in this field are mentioned in literature, for example about a straight DBD [13], indicating that the best drag reduction is achieved by introducing small flow scales in the boundary layer, whereas the generation of larger structures ($F_+ \sim 1$) is more useful for lift control. In this case, the numerous tips of C6 could presumably help this device in introducing the small scales mentioned above, however also the passive effect is important, in fact all the values of $<\Delta c_d>_t$ are higher and the top value corresponds to C13, nearly equal to C6. Finally, it is worth to mention that the search for an optimal drag is particularly sensitive to the control parameters: indeed, the $<\Delta c_d>_p$ scale ranges from -6% to +9%, since in some regions of the F_+, D_c plane the actuators can also produce a mean drag increase.

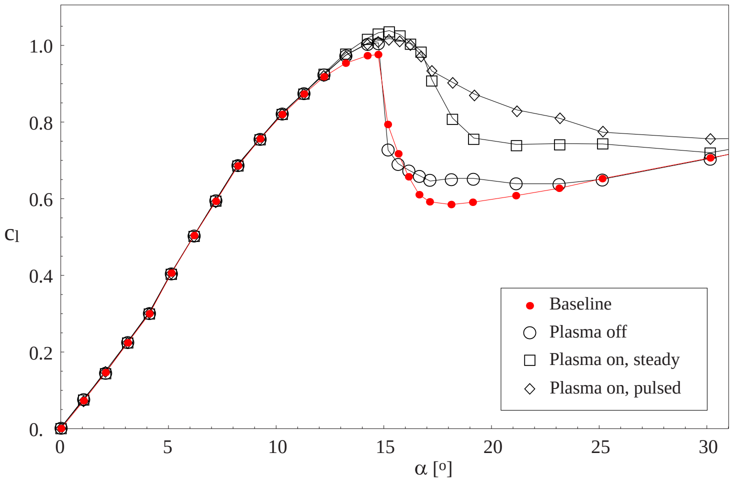

(a) Lift coefficient.

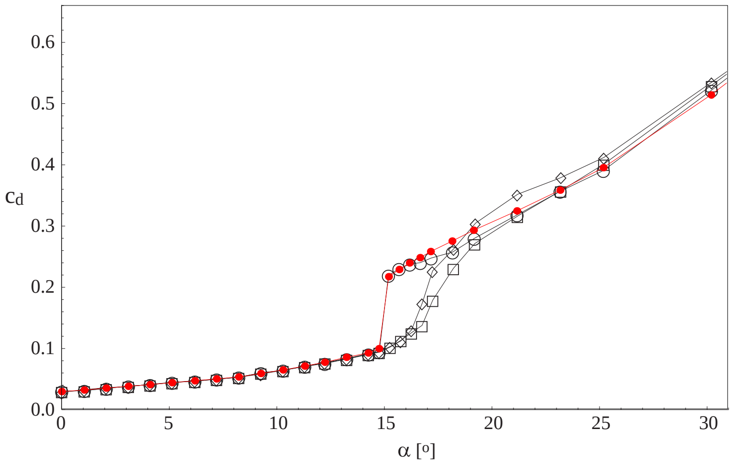

(b) Drag coefficient.

Figure 13: Actuator C6, aerodynamic coefficients vs α at U=20 m/s: baseline, plasma off, steady plasma and pulsed plasma with $(F_+, D_c) = (1, 0.1)$.

3.4. BL measurements

In this section, further measurements are carried out by exploring the velocity profiles in the boundary layer downstream of the actuators. The velocities are obtained by means of a small pitot probe as described in the setup section. The measurement grid is sketched in Fig. 15: over the surface of the airfoil, up to three distances downstream of the actuators have been considered, $s_1, s_2, s_3 = 17, 25, 40$ mm along the surface from the tips line - coincident with the leading edge - or $x_1, x_2, x_3 = 12.1, 19.8, 34.5$ mm along the chord. The distances from the tips line s_1=17 mm and $s_3 = 40$ mm are the same used for previous measurements at the bench on the same coronas [6]. For each chordwise position, several velocity profiles have been acquired at different spanwise locations, behind tips, roots and intermediate points. Fig. 15 refers to a multi-tip corona, and becomes simpler for the wire-plate C1, where it is not necessary to consider the dependence on the span coordinate z.

These measurements are mainly devoted to assess the capability of the actuators in injecting momentum, so they have been acquired with steady driving ($D_c = 1$). The airstream velocity has been set as above to 20 m/s and the angle of attack to 13° in order to have conditions where the effect of the actuators is measurable but the separation has not completely taken place.

The knowledge of a given velocity profile $u(y)_z$ for a given spanwise location makes possible to calculate a local momentum coefficient

$$c_{\mu,z} = \frac{2}{U^2 c} \int_0^{y_m} (u_{on}^2 - u_{off}^2)_z \, \mathrm{d}y \tag{12}$$

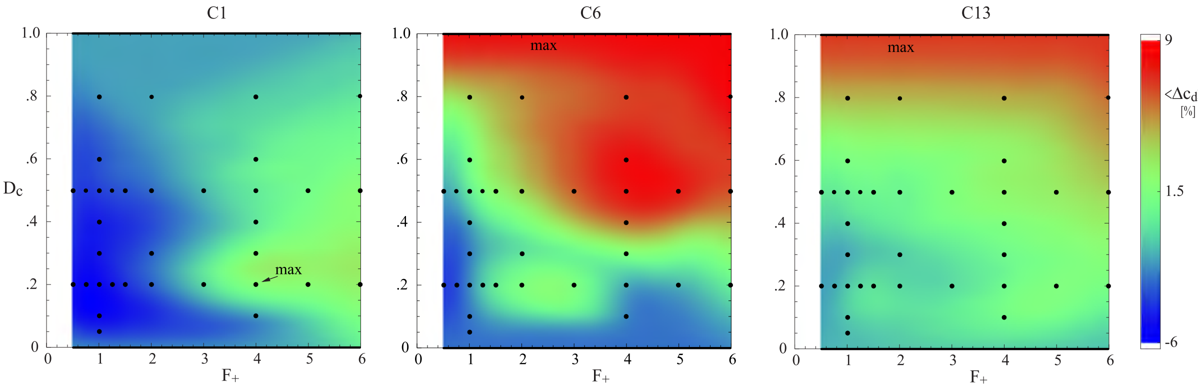

Figure 14: Maps of $<\Delta c_d>_p$ as function of F_+ and D_c. The maxima are explicitly indicated.

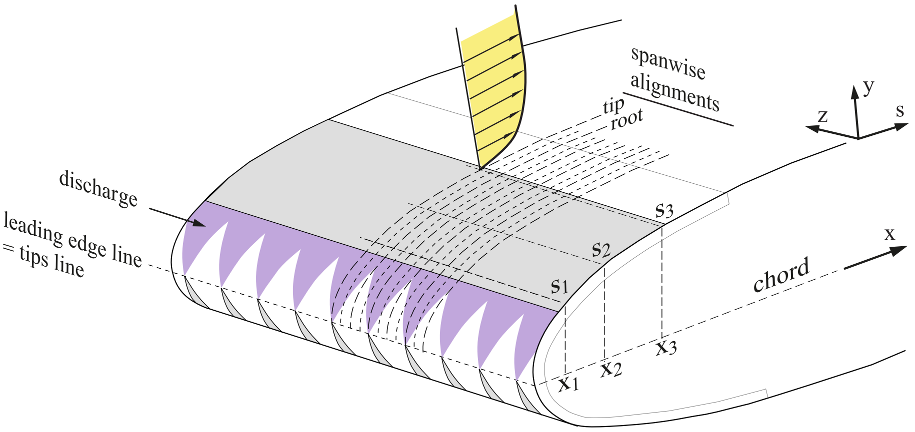

Figure 15: BL velocity measurements: selected chordwise and spanwise locations of the probe. The sample velocity profile is not to scale for clarity.

based on the velocity increase u_{on} to u_{off}, integrated up to the last measurement point y_m. In turn, repeating the measurements over different spanwise alignments (tip-intermediate-root-intermediate...), a spanwise-averaged coefficient c_μ can be calculated for each multi-tip actuator, to be compared with the value determined for the reference wire-plate configuration. Here c_μ is made dimensionless by the airstream velocity U and the chord c, although a different choice (e.g. the BL thickness) is possible. The resulting momentum coefficients are shown in Table 5 for two chordwise distances, including also the local values $c_{\mu,tip}$ in order to evidence the local variations.

Table 5: Momentum coefficients at 2 distances downstream of the leading edge.

	s_1=17mm		s_3=40mm	
Actuator	c_μ [%]	$c_{\mu,tip}$ [%]	c_μ [%]	$c_{\mu,tip}$ [%]
C6	0.42	0.45	0.14	0.16
C13	0.14	0.55	0.11	0.46
C1	0.20	–	0.05	–

The accuracy of the data in Table 5 is very different for the two chordwise distances: in fact, for $s = s_1$ the measurements are more influenced by the unsteady reattachment of the recirculation bubble just upstream of the test point, particularly when the actuators are off. This leads to uncertainties in the order of $\pm 0.08\%$ on the c_μ values at s_1, whereas the data for $s = s_3$ have uncertainties in the order of $\pm 0.02\%$. Along the surface, as s (or x) grows, the measured coefficients decrease because of the momentum consumption at the wall; at the same time, the momentum diffuses in the surrounding flow region as the flow develops downstream. These phenomena affect C6 and C13 to different extents: for C6, the high momentum behind the tips at $s_1 = 17$mm is rapidly diffused across the short tip spacing, leading to a nearly uniform effect at $s_3 = 40$mm. For C13 instead, $c_{\mu,tip}$ is higher than for C6 along the whole range of distances s_1 to s_3, but the average value is lower, since these powerful tips are isolated from each other.

The results of the previous section indicate as most promising actuator the corona C6, that maintains a good performance at the same time for early and deep stall: comparing this performance with the data in Table 5, it is concluded that energizing the boundary layer by a spanwise distributed momentum (C6) or by intense isolated jets (C13) is equally effective for early stall control, whereas for deep stall control the distributed momentum effect becomes the best choice.

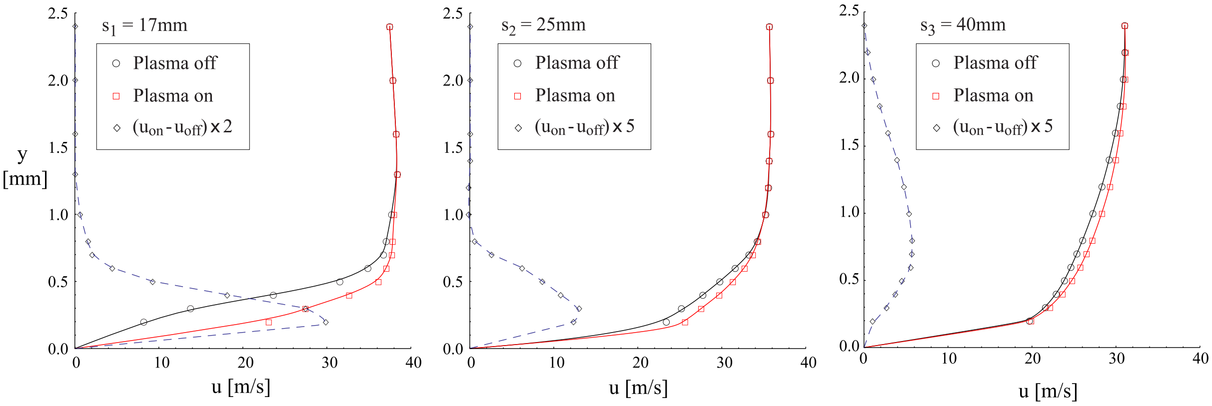

Figure 16: BL velocity profiles for C6, aligned to a tip at 3 surface distances s_1, s_2, s_3. On-off differences shown on a magnified scale.

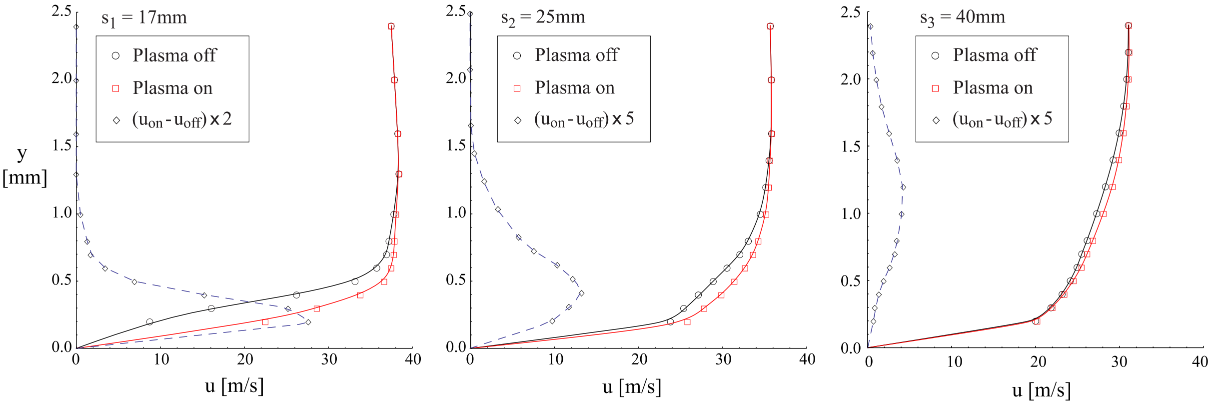

Figure 17: BL velocity profiles for C6, aligned to a root at surface distances s_1, s_2, s_3. On-off differences shown on a magnified scale.

The detailed description of the boundary layer modifications created by C6 is given in what follows. As sketched in Fig. 15, for each chordwise position, several velocity profiles have been acquired at different spanwise locations and used to determine mean profiles for the 3 spanwise alignments (tip-intermediate-root). The total spanwise field, explored around the tunnel centerline, is 20 mm corresponding to 5λ in terms of tips spacing. In Fig. 16, 3 pairs of on-off velocity profiles downstream of a tip, obtained as mean values of repeated tests, are presented at distances s_1, s_2, s_3 from the corona anode (leading edge). The figure include plots of the differences $u_{on} - u_{off}$ to evidence the discharge effect. With plasma off, at s_1 the thickness is δ^*=0.36 mm and the shape factor is $H = 3.2$, indicating a laminar boundary layer close to separation, which is consistent with the visualization of Fig. 8, since this location is affected by the unsteady reattachment of the laminar bubble: upstream of this point the instantaneous velocity profile presumably fluctuates between separated and attached. At s_2, the thickness decreases to δ^*=0.25 mm and the shape factor to $H = 2.0$, indicating that the transition to turbulence is taking place, and finally at s_3, the thickness increases again to δ^*=0.36 mm with $H = 1.7$, values compatible with a turbulent boundary layer. With plasma on, all the profiles exhibit local velocity increases, and the BL thicknesses decrease to δ^*=0.22, 0.22 and 0.32 mm respectively. The shape factor at s_1 drops to H =2.3, indicating that the BL is stably attached, whereas at s_2 and s_3 the H parameter does not change, and remains nearly insensitive to the plasma effect.

Due to the diffusive effects on the short tip spacing, the profiles at different spanwise positions are not much different: in fact, the profiles behind the roots visible in Fig. 17 are similar to the ones reported behind the tips, confirming that the momentum generated by the tips is rapidly distributed over the small inter-tip distance. In other words, the flow structure generated by this actuators is quite simple, the actuator behaves as a full-span momentum injector and it is easy to collect the data to calculate spanwise-averaged values for the integral parameters: along the 3 positions s_1 to s_3, the average δ^* evolves as the local values reported above, taking on the values 0.35, 0.26, 0.36 mm with plasma off and 0.22, 0.22, 0.33 mm with plasma on.

4. Conclusions

In this work, two coronas with multiple triangular tips on their anodes have been tested in the wind tunnel to determine their performance in controlling a separated flow, by operating them in a new mode, based on a periodic waveform of positive voltage. This waveform, with respect to a standard DC supply, leads to a great improvement in the operability of these devices. The main (carrier) frequency can also be modulated by a slower frequency, and this permits to obtain steady and pulsed actuations, as usually done for the well known DBD actuators.

The two multi-tips have been selected out of a larger set on the basis of previous investigations: one actuator has numerous adjacent tips, the other one few isolated tips. All the tests have been repeated on a standard wire-plate corona as a reference. The two multi-tips perform better than the wire-plate in all the tests: stall inception control, deep stall control and drag reduction.

As reported in literature about similar experiments with DBDs, the largest lift increase at stall inception is obtained by steady actuation. These results, related to the momentum injection in the early boundary layer, can be obtained both by the corona with numerous adjacent tips and by the corona with isolated tips. In deep stall control, low modulation frequencies (dimensionless values F_+ from 0.5 to 1) become the best effective choice, rising the lift curve over a wide range of angles of attack above the stall inception value α_c. This control can be obtained by short duty cycles, leading to a good power saving. In this flow regime, the corona with isolated tips is no longer effective, and the best geometry seems to be the one with numerous adjacent tips, presumably because a well distributed momentum injection is more suitable to create periodical spanwise structures and control the vortex shedding in the separated region. The above considerations confirm the excitation of spanwise vortical structures as an effective control mechanism in deep stall, requiring relatively low frequencies to be successful. The results in early stall regime instead could need further investigation to determine beyond any doubt if the main mechanism is more related to the transition excitation or to a circulation enhancement driven by the momentum injection. Finally, the best drag reduction is obtained either by steady actuation or by pulsing the waveform at high frequencies ($F_+ \geq 4$), with relatively high duty cycles.

As a further remark, it is worth to note that when the managed power requires a not negligible electrodes thickness with respect to the local boundary layer, the passive effects of the actuators should be carefully considered. In fact, at the present Reynolds number (330k) the electrodes can affect the boundary layer development, and it is expected that at lower numbers the unpowered actuators may play a great role in the transition to turbulence, whereas for sufficiently larger Reynolds numbers the actuators should operate in a boundary layer which is already turbulent in the baseline flow. To account for the effects above, the results have been presented in two ways, reporting I) the total effects, i.e. the aerodynamic changes due to the installation of a powered actuator on a smooth airfoil. II) the relative (plasma) effects due to discharge only, i.e. the aerodynamic changes when an already installed actuator is switched on. In general, in this experiment the unpowered actuators have favourable passive effects improving the transition to turbulence, so that the performance of type I) appears better than for type II).

In literature, the coronas are widely recognized as efficient devices, and in this study they reach even higher efficiencies, thanks to the very short effective duty cycle: in fact, as shown in Fig. 4, the actuators are on for short periods only, corresponding to the wave crests of the driving voltage. For the same reason, they become also easier to ignite and manage, with less undesired sparks and a reduced sensitivity to the external environment, even if the DBD performance with very high humidities can not be reached. In conclusion, the present results indicate that corona actuators of suitable geometry, operated with repetitive waveforms similarly to the DBDs, can give an interesting performance with high efficiency, at least where the environmental conditions can be controlled, as in the case of curved surfaces inside ducts, for example in wind tunnel flows.

[1] Forte, M., Jolibois, J., Pons, J., Moreau, E., Touchard, G., and Cazalens, M., "Optimization of a dielectric barrier discharge actuator by stationary and non-stationary measurements of the induced flow velocity: application to airflow control," *Experiments in Fluids*, Vol. 43, No. 6, 2007, pp. 917–928.

[2] Thomas, F. O., Corke, T. C., Iqbal, M., Kozlov, A., and Schatzman, D., "Optimization of dielectric barrier discharge plasma actuators for active aerodynamic flow control," *AIAA journal*, Vol. 47, No. 9, 2009, pp. 2169–2178.

[3] Durscher, R., and Roy, S., "Induced flow from serpentine plasma actuators acting in quiescent air," *49th AIAA Aerospace Sciences Meeting*, Orlando, Florida, 4–7 January 2011, AIAA 2011-957, pp. 1–11.

[4] Berendt, A., Podlinski, J., and Mizeraczyk, J., "Comparison of airflow patterns produced by DBD actuators with smooth or saw-like discharge electrode," *Journal of Physics: Conference Series*, Vol. 301, No. 1, 012018, 2011, pp. 1–4.

[5] Joussot, R., Leroy, A., Weber, R., Rabat, H., Loyer, S., and Hong, D., "Plasma morphology and induced airflow characterization of a DBD actuator with serrated electrode," *Journal of Physics D: Applied Physics*, Vol. 46, No. 12, 2013.

[6] Belan, M., and Messanelli, F., "Compared ionic wind measurements on multi-tip corona and DBD plasma actuators," *Journal of Electrostatics*, Vol. 76, 2015, pp. 278–287.

[7] Messanelli, F. and Belan, M., "Ionic wind measurements on multi-tip plasma actuators," *EPJ Web of Conferences* 114, 02073, 2016, pp. 1–8.

[8] Belan, M., and Messanelli, F., "Wind tunnel testing of multi-tip corona actuators on a symmetric airfoil," *Journal of Electrostatics*, Vol. 85, 2017, pp. 23–34.

[9] Messanelli, F., and Belan, M., "A Comparison Between Corona and DBD Plasma Actuators for Separation Control on an Airfoil," *55th AIAA Aerospace Sciences Meeting, AIAA SciTech Forum*, Grapevine, Texas, 9–13 January 2017, AIAA 2017-0395, pp.1–14.

[10] Benard, N., Braud, P., Jolibois, J., and Moreau, E., "Airflow reattachment along a NACA 0015 airfoil by a surface dielectric barrier discharge actuator time-resolved particle image velocimetry investigation," *4th Flow Control Conference*, Washington, Seattle, 23–26 June, 2008, AIAA 2008–4202.

[11] Benard, N., Jolibois, J., and Moreau, E., "Lift and drag performances of an axisymmetric airfoil controlled by plasma actuator," *Journal of Electrostatics*, Vol. 67, No. 2, 2009, pp. 133–139.

[12] Kelley, C. L., Bowles, P., Cooney, J., He, C., Corke, T. C., Osborne, B., Silkey, J., and Zehnle, J., "High Mach number leading-edge flow separation control using AC DBD plasma actuators," *50th AIAA Aerospace Sciences Meeting*, Nashville, Tennessee, 9–12 January, 2012, AIAA 2012–0906.

[13] Kelley, C. L., Bowles, P. O., Cooney, J., He, C., Corke, T. C., Osborne, B. A., Silkey, J. and Zehnle, J., "Leading-edge separation control using alternating-current and nanosecond-pulse plasma actuators," *AIAA Journal*, Vol. 52, No. 9, 2014, pp. 1871–1884.

[14] Barlow, J. B., Rae, W. H., and Pope, A., "Low-speed wind tunnel testing," *John Wiley and Sons*, 1999.

[15] Garner, H. C., Rogers, E. W., Acum, W. E., and Maskell, E. C., "Subsonic wind tunnel wall corrections," No. AGARD-OGRAPH-109, Advisory group for aerospace research and development (AGARD), Neuilly-Sur-Seine (France), 1966.

[16] Messanelli, F., "Optimization of plasma actuators for flow control," PhD dissertation, PhD School of Politecnico di Milano, 2018, http://hdl.handle.net/10589/137301

[17] Kriegseis, J., Möller, B., Grundmann, S., and Tropea, C., "Capacitance and power consumption quantification of dielectric barrier discharge (DBD) plasma actuators," *Journal of Electrostatics*, Vol. 69, 2011, pp. 302–312.

[18] Melton, L. P., Hannon, J., Yao, C. S., and Harris, J., "Active flow control at low Reynolds numbers on a NACA 0015 airfoil," *26th Applied Aerodynamics Conference. Number AIAA*, Vol. 6407, August 2008.

[19] He, C., Corke, T. C., and Patel, M. P., "Plasma flaps and slats: an application of weakly ionized plasma actuators," *Journal of Aircraft*, Vol. 46, No. 3, 2009, pp. 864–873.

[20] Mabe, J.H., Calkins, F.T., Wesley, B., Woszidlo, R., Taubert, L., and Wygnanski,I., "Single Dielectric Barrier Discharge Plasma Actuators for Improved Airfoil Performance", *Journal of Aircraft*, vol. 46, no. 3, 2009, pp. 847–855.

[21] Drela, M., and Giles, M. B., "Viscous-Inviscid Analysis of Transonic and Low Reynolds Number Airfoils," *AIAA Journal*, Vol. 25, No. 10, 1987, pp. 1347–1355.